Frit-inlet asymmetric flow field-flow fractionation for the analysis of lipid nanoparticle-protein interactions

Rand Abdulrahman [a], Panida Punnabhum [a], Robin Capomaccio [b], Kevin Treacher [b], Yvonne Perrie [a], Zahra Rattray [a,*]

[a] Strathclyde Institute of Pharmacy and Biomedical Sciences, University of Strathclyde, Glasgow, UK
[b] New Modalities Product Development, Pharmaceutical Technology & Development, Operations, AstraZeneca, Macclesfield, UK

ABSTRACT

Research into nanoparticle interactions with biomolecules has become increasingly important in nanomedicine. While lipid nanoparticles (LNPs) are widely used as drug delivery systems, there remains a gap in understanding their fate in circulation, which is crucial for selecting appropriate lipids during formulation development. This study is the first to use Asymmetric Flow Field Flow Fractionation (AF4) to compare two types of LNPs: MC3-LNPs and SM-102-LNPs, and their interactions with a model protein, bovine serum albumin (BSA). AF4 offers high-resolution separation, with the ability to simultaneously perform multiparametric inline analysis with multiple detectors. In this study, the impact of LNP size, morphology and PDI on BSA corona formation were examined using inline multiangle light scattering (MALS) and dynamic light scattering (DLS). AF4 separation revealed two subpopulations for MC3-LNPs, while SM102-LNPs exhibited a single population. Analysis of shape factor indicated a shape factor of 0.783 for SM-102-BSA and 0.741 and 0.795 (peak 1 and 2) for MC3-BSA, confirming interaction between LNPs and BSA. Both LNPs exhibited LNP-BSA induced aggregation. Overall, this study demonstrates the effectiveness of AF4, particularly when hyphenated with multidetector systems, for simultaneously separating LNPs from complex biological media and studying LNP-protein interactions.

1. Introduction

mRNA-based therapies, which target disease-related proteins to alter their expression and function, have gained traction as a strategy for treating disease. [1] While lipid nanoparticles (LNPs) have proven to be an effective drug delivery system, particularly highlighted by their success in COVID-19 immunisation efforts, the interactions between LNPs and biological systems have not been thoroughly explored. Following administration, depending on the route of administration, various proteins from the subcutis interstitial fluid and blood serum spontaneously adsorb onto the LNP surface, forming a complex termed the 'protein corona'. [2–4] This protein corona is critical in determining how LNPs interact with biological systems. The formation of the protein corona can alter the LNP surface, impacting its biological activity, including its biophysical characteristics in the presence of surface-adsorbed biomolecules. These changes can modify LNP physical properties, organ biodistribution, physicochemical stability, cellular uptake and circulation time. As a result, the behaviour and effectiveness

of LNPs can significantly vary [5–9].

The fate of LNPs is influenced by the composition of surface-adsorbed proteins, and the physicochemical changes induced by the biomolecular corona can be correlated with different LNP constituents (Fig. 1). Ionisable cationic lipids are particularly important for LNP function. Efforts to optimise these cationic lipids for siRNA delivery have led to the development of lipids that are now incorporated into clinically approved LNPs [10,11]. DLin-MC3-DMA (heptatriaconta-6,9,28,31-tetraen-19-yl-4-(dimethylamino)butanoate) and SM-102 (heptadecan-9-yl 8-((2-hydroxyethyl) (6-oxo-6-(undecyloxy) hexyl) amino) octanoate) are two clinically-approved ionisable lipids used in Onpattro® (Alnylam Pharmaceuticals) and SpikeVax® (Moderna), respectively [12,13].

Asymmetric Flow Field-Flow Fractionation (AF4) is emerging as a valuable technique in the field of nanomedicine due to its low-stress and non-disruptive separation capabilities [14–20]. AF4 can be coupled with multiple detectors to analyse various LNP critical quality attributes such as particle size, polydispersity, and molecular weight. Multi-angle light scattering is used to measure the molar mass and size of particles, often

expressed as the radius of gyration (R_g). In conjunction with R_g, the Stokes radius or hydrodynamic radius (R_h) can be determined using inline dynamic light scattering (DLS). The combination of these measurements allows for the assessment of particle shape factor (R_g/R_h). [21] A key advantage of AF4 for protein corona analysis is its ability to characterise particles *in situ* without the need for prior separation of unbound proteins. This avoids potential alterations to nanoparticle parameters that may occur with commonly used methods such as centrifugation-resuspension [22,23]. AF4 to-date has offered valuable insights into the improvement of loop-mediated isothermal amplification and lateral flow assay (LAMP-LFA) [24–26]. A recent study by Safenkova et al. demonstrated the usefulness of AF4 in characterising nucleic acid amplification. [27]

Although emerging publications demonstrate the use of AF4 for analysing LNP formulation stability, there is a notable lack of studies focusing on AF4 applications for the separation and online analysis of LNPs in biological media. This study aims to understand different interactions of two model LNP prototypes with different ionisable lipid composition (MC3 and SM-102) with Bovine Serum Albumin (BSA) as a model protein contained in biological media in cell-based assays. This work lays the foundation for future studies on LNP biomolecule-nanomaterial interactions using a high-resolution characterisation and gentle separation technique, which is critical for soft LNP materials.

2. Materials and methods

2.1. Reagents and materials

Polyadenylic acid (PolyA), cholesterol, sodium citrate dihydrate, ethanol, and dialysis tubing cellulose membrane (molecular weight cut-off size 14 kDa) were purchased from Sigma-Aldrich (St. Louis, MO, USA). Helper lipids 1,2-distearoyl-sn-glycero-3-phosphocholine (DSPC), 1,2-dimyristoyl-rac-glycero-3-methoxypolyethylene glycol-2000 (DMG-PEG 2000) were purchased from Avanti Polar Lipids (Alabaster, AL,

USA). The ionisable lipids (6Z,9Z,28Z,31Z)-Heptatriaconta-6,9,28,31-tetraen-19-yl 4-(dimethylamino)butanoate (D-Lin-MC3-DMA) and 8-[(2-hydroxyethyl)[6-oxo-6-(undecyloxy)hexyl]amino]-octanoic acid, 1-octylnonyl ester (SM-102) were purchased from BroadPharm (San Diego, CA, USA). Lyophilised powder Bovine Serum Albumin (BSA), Invitrogen™ UltraPure™ DNase/RNase-Free Water and Phosphate-buffered saline (PBS) 10X salt solution pH 7.4 was acquired from Fisher Scientific (Loughborough, UK).

2.2. Synthesis of lipid nanoparticles

Poly(A) lipid nanoparticles (LNPs) were manufactured using the NanoAssemblr® Ignite Precision NanoSystems (Vancouver, BC, Canada) using the NxGen microfluidic cartridge, which uses a toroidal mixer. Lipid stocks were prepared in ethanol at molar ratios 50:38.5:10:1.5 for d-Lin-MC3-DMA/SM102: Cholesterol: DSPC: DMG-PEG 2000, which is based on the lipid compositions of Onpattro® and Comirnaty®. [28] The aqueous phase consisted of initial Poly(A) stock at 1.5 mg/mL dissolved in 50 mM citrate buffer (pH 4.0). The Total Flow Rate (TFR) was set at 15 mL/min, and an aqueous-to-organic Flow Rate Ratio (FRR) of 3:1 was used with a final lipid concentration of 1.25 mg/mL and Poly(A) of 0.055 mg/mL. The N:P (N for lipid nitrogen and P for nucleic acid phosphate) was 6:1. LNPs were purified by dialysis to remove ethanol and citrate buffer. Resultant suspensions were dialysed at 4 °C (MWCO 14 kDa, Sigma-Aldrich, St. Louis, MO, USA) into 1X phosphate buffered saline (PBS, pH 7.4) (500X dialysate ratio) to remove ethanol and citrate buffer. All formulations were syringe-filtered through 0.2 µm pore-sized Supor® membrane (Pall Corporation, USA) and stored at 4 °C until further use.

2.3. Sample preparation

MC3 and SM102 LNPs were incubated with Bovine Serum Albumin (BSA), which was used as a model protein to study LNP-BSA corona
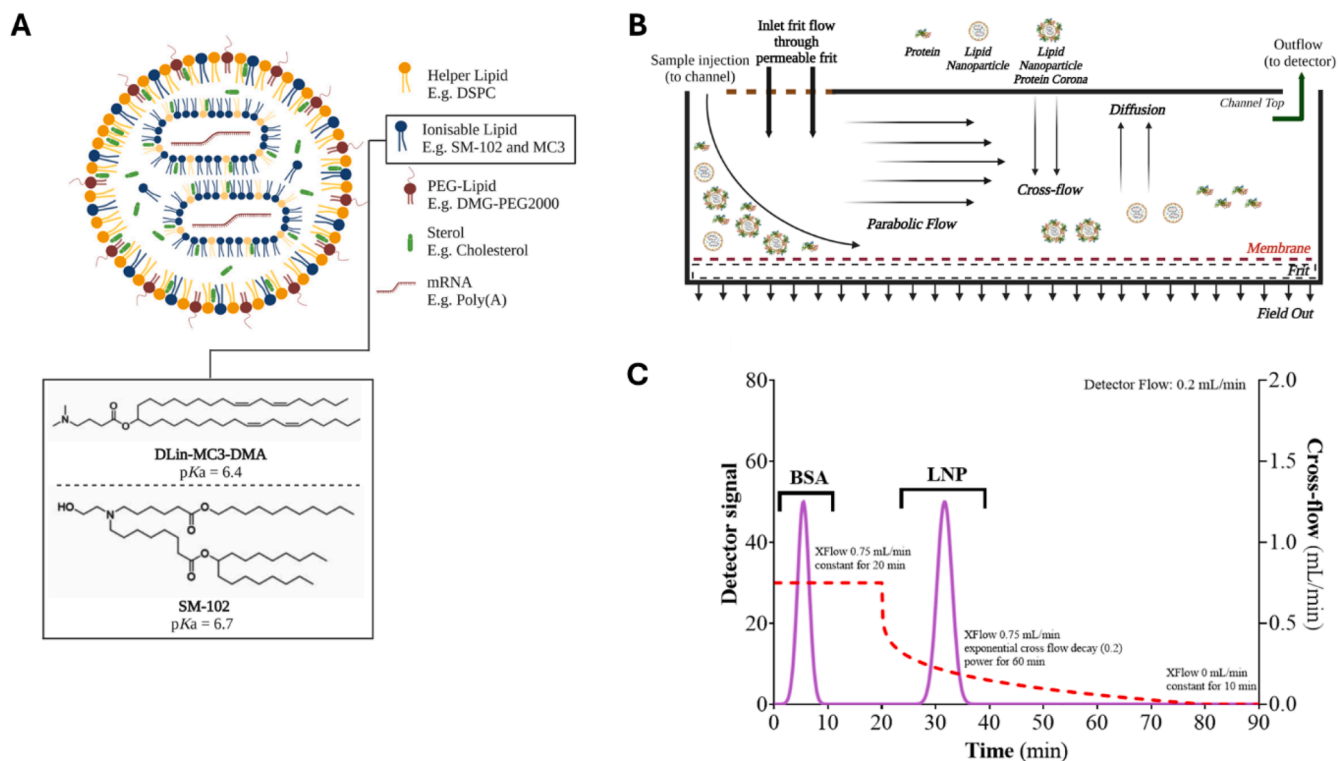

Fig. 1. Schematic showing formation (A) Lipid nanoparticles (LNP) components with difference in ionisable lipids (D-Lin-MC3-DMA referred as MC3 and SM-102), (B) Side-view of frit-inlet AF4 channel with protein, LNP and LNP-protein corona in the channel and (C) a representative simulated AF4 profile of Bovine Serum Albumin (BSA) and LNP with the applied cross-flow (XFlow) and detector signal (A) and (B) created with BioRender.com and (C) NovaAnalysis software.

formation. MC3-LNP and SM-102 LNPs were incubated at a 1:1 (volumetric ratio) with BSA (35 mg/mL in PBS (pH 7.4)), and the mixture was incubated for 24 h at 37 °C in Protein LoBind eppendorfs. Control samples included an equal volume of PBS and LNP.

2.4. Dynamic light scattering

Samples were analysed using a Zetasizer Nano ZS (Malvern Panalytical, Malvern, Worcestershire, UK) to obtain particle size and Polydispersity Index (PDI) for control (LNP in PBS) at 0 h. All measurements were performed at 25 °C using the non-invasive backscattering setting (NIBS, 173°) at a dilution of 1:10 in PBS (pH 7.4). Final measured sample concentrations were theoretical lipid concentration of 125 μg/ mL and Poly(A) concentration of 5.5 μg/mL. All measurements were performed in three independent replicates and at least three technical replicates.

2.5. Electrophoretic light scattering (ELS)

The ζ-potential of LNP-Control and LNP Corona was measured by electrophoretic light scattering at 25 °C and the Smoluchowski approximation was used. All measurements were performed at 25 °C using non-invasive backscattering (NIBS, 173°) at a dilution of 1:10 in DNA/RNA free water for control (LNP-PBS) at 0 h. All measurements were performed in three independent replicates and five technical replicates.

2.6. Encapsulation efficiency (EE)

The encapsulation efficiency of LNPs was determined using Quant-iT™ RiboGreen RNA Assay Quantitation (Invitrogen™, Thermo Fisher Scientific, UK) as per manufacturer's instructions and previously reported. [29]

2.7. Frit-Inlet asymmetric flow field-flow fractionation

A Postnova Analytics AF2000 asymmetric Flow Field-Flow Fractionation (AF4) (Landsberg, Germany) was used in this study. The system was configured with tip and pressure pumps, a degasser, and autosampler. The system was configured with online UV–Vis (PN3242, 260 nm- PostNova Analytics) and a 21-angle Multi-angle Light Scattering (MALS-PN3621, Postnova Analytics), and online Zetasizer Nano ZS (Malvern Panalytical, Malvern, UK) detector integrated into the system. AF4-based separation and inline analysis was performed using a frit-inlet rectangular channel (300 × 60 × 40 mm) assembled with a trapezoidal geometry, (spacer thickness 350 μm). The membrane used was a 10 kDa molecular weight cut-off (MWCO) size amphiphilic regenerated cellulose (RC) membrane, with a 100 μL injection loop size and a 20 μL sample injection volume. The compatibility and the pore size (MWCO, molecular weight cut-off) of the membrane is crucial since sample fractionation occurs close the membrane. Binding between the RC membrane and analytes was assumed to be negligible with minimal sample adsorption to membrane.

PBS (10 mM, pH 7.4) was used as the carrier liquid. The corresponding detector flow (DF), and cross-flow (XF) settings were based on previously-reported parameters, with DF set at 0.2 mL/min, and cross-flow initiated with 0.75 mL/min held for 20 min, followed by an exponential decrease from 0.75 mL/min to 0 mL/min for 60 min, and held at 0 mL/min for 10 min. [20] The cross-flow rate is the defining factor for separation. As the cross-flow pushes analytes to the accumulation wall, analytes diffuse in the counter direction by Brownian motion according to their diffusion coefficients. A high cross-flow improves resolution but also increases the risk of analyte adsorption on the bottom wall due to closer proximity to the accumulation wall. In this study, a relatively low cross-flow was used, which allowed for analyte separation and acceptable mass recovery.

Online DLS measurements were acquired using a Malvern quartz

flow cell (ZEN0023), at a flow rate of 0.2 mL/min at 25 °C at three-second intervals. The measurement position was set at 4.2 mm with the attenuator set at 11.

Mass recovery for the LNP and LNP-BSA complex at 0 and 24 h were determined using the below equation (UV signal at 260 nm):

$$R(\%) = \frac{A_c}{A} \; x \; 100 \tag{1}$$

Where A_c is the area under the peak of nanoparticles under a cross-flow, and A is the area under the peak of the unfractionated sample without an applied cross-flow *via* direct sample injection. Corresponding shape factor was calculated using the following equation:

$$\rho = \frac{R_g}{R_h} \tag{2}$$

where ρ is the shape factor, R_g represents the radius of gyration (nm) obtained from MALS detector and R_h represents the hydrodynamic radius (nm) obtained from DLS detector.

Mean and standard deviation of the R_g, R_h and shape factor was calculated by averaging the points obtained across the full-width half maximum (FWHM) of the eluting peak. Outside the FWHM, noisy DLS data were detected, which were excluded from the average. The FWHM was determined by first identifying the maximum signal intensity. Next, the two points on the peak, where the intensity occurs at half the maximum value were located on the x-axis. The distance between these two points was determined as the FWHM.

2.8. Statistical analysis

Statistical analysis was performed with one-way ANOVA followed by Tukey's multiple comparisons test for post-hoc analysis. Statistical significance was considered at $p < 0.05$; *$p < 0.05$, **$p < 0.01$, ****$p < 0.0001$. All data were analyzed using GraphPad Prism 8 (GraphPad Software Inc) and were expressed as mean ± SD ($n = 3$). Cumulative frequency distribution plots for RG (radius of gyration), RH (hydrodynamic radius) and SF (shape factor) were plotted using cumulative distribution function on GraphPad Prism 8. The percentile values 10 %, 50 % and 90 % of the distributions were calculated using the TREND function on Microsoft Excel.

3. Results

3.1. Characterissation: particle size, zeta potential, PDI and enapsulation efficiency

Initial baseline analysis of particle size, PDI and zeta potential was measured using batch-mode DLS of LNP prototypes (lipid concentration of 1.25 mg/mL) prior to incubation in BSA using cumulant algorithm analysis accepted by ISO standards for particle size (ISO 13,321). Both LNPs resulted in a measured Z-average < 100 nm (74.9 ± 2.6 nm and

Table 1

Baseline Critical Quality Attributes (CQAs) quantified for MC3, SM-102 LNPs and Bovine Serum Albumin (BSA). Z-Average and polydispersity index (PDI) were measure using DLS cumulant algorithm analysis and ELS for the measurement of zeta potential. Poly (A) encapsulation efficiency was measured using the RiboGreen™ RNA Assay. Data are shown as mean ± SD, n = 3.

Sample	Z-Average (nm)	PDI	Zeta Potential (mV)	Enapsulation Efficiency (%)
BSA	7.5 ± 0.0	0.131 ± 0.009	−12.3 ± 4.6	–
MC3 LNPs	74.9 ± 2.6	0.152 ± 0.010	−7.6 ± 2.6	98 ± 2
SM-102 LNPs	67.7 ± 0.6	0.165 ± 0.069	−5.6 ± 2.3	96 ± 2

67.7 ± 0.6 nm for MC3 and SM-102, respectively) (Table 1). The corresponding PDI showed homogenous LNP prototypes (0.152 ± 0.010 in the case of MC3 and 0.165 ± 0.069 for SM-102). Both prototypes were negatively charged in formulation buffer (pH 7.4), with encapsulation efficiency measured at > 95 % for both prototypes.

3.2. Hydrodynamic radius (R_h) and radius of gyration (R_g) in response to incubation with BSA

Previous studies using cryogenic transmission electron microscopy (cryo-TEM) have reported a spherical morphology of ionisable cationic lipid nanoparticles [30–32]. Therefore, a spherical model was applied to fit the MALS data (36°-156°), with representative LNP fractograms presented in **Figure S1**. Recovery data (SI S2 and S3) showed excellent recovery for LNPs at $t = 0$ for MC3 LNPs (97 ± 2%) and SM-102 LNPs (111 ± 13%). The MALS trace indicated a BSA peak eluting at ~ 5 min and LNP (control) / LNP-BSA peaks eluting around 25–30 min (Fig. 2). Fig. 2**A-B** (LNP-BSA at 24 h) shows a reduction in UV signal for the LNP peak due to the high absorption of the amino acid residues in BSA. On the contrary, Fig. 2**C-D** (LNP-BSA at 24 h) exhibited a lower MALS signal for BSA compared to LNP, due to more light scattering from larger LNPs. MC3-LNPs displayed peak splitting with differences in R_g and R_h between the two sub-populations at 0 h. In contrast, SM-102 LNPs exhibited a single peak for both MALS and UV signals. A reduction in MALS signal intensity was observed for SM-102 LNPs, with less than a 10 % difference across all incubations. In contrast, MC3 LNPs showed a noticeable increase in intensity with MC3-BSA after 24 h of incubation.

An increase in Rg and Rh values along the sample elution was observed for both LNP prototypes, with a higher increase Rg and Rh for MC3-LNPs compared to SM-102 LNPs which indicates polydispersity of MC3-LNP samples (Fig. 3A-B). Fig. 3C-D displays the cumulative RG (radius of gyration) distributions for RG10, RG50, RG90 and Fig. 3E-F as a function of RH (radius of hydration). There was a significant reduction in RH90 between SM-102-PBS (34.6 ± 0.4 nm) and SM-102-BSA (33.3 ± 0 nm) for 24 h incubation. However no significant difference was seen between these two samples in the case of RG. A non-significant lower RG90 (26.3 ± 1.2 nm) for SM-102-BSA at 24 hour was shown. The error bars for the Rg distribution of SM-102 LNPs overlap between SM-102-PBS and SM-102-BSA at 24 h incubation indicating non-significance (Fig. 3D). This is compared to MC3-LNP incubations showing small variations in cumulative distribution curves (Fig. 3C). Average Rh and Rg results show that following a 24 h incubation, a significant difference was observed in average Rh for the second subpopulation (39.8 ± 0.0 nm to 38.9 ± 0.2 nm for MC3-PBS and MC3-BSA, respectively), while Rg for peak 1 increased significantly (17.6 ± 0.4 nm to 19.0 ± 0.2 nm for MC3-PBS and MC3-BSA, respectively) (Fig. 4 and Table S4). SM-102 LNPs showed a significant increase in Rg between SM-102-PBS at 0 hour and 24 h (22.9 ± 0.2 nm to 24.1 ± 0.3 nm respectively) and a significant reduction in Rg between SM-102-PBS at LNP-BSA at 24 h (24.1 ± 0.3 nm and 23.0 ± 1.0 nm, respectively) (Fig. 4 and Table S4).

3.3. Quantification of MC3 and SM-102 LNP geometry and polydispersity in response to incubation with BSA

The shape factor for an ideal solid sphere is approximately 0.77. [21] Shape factors > 0.77 indicate a deviation from sphericity or uneven
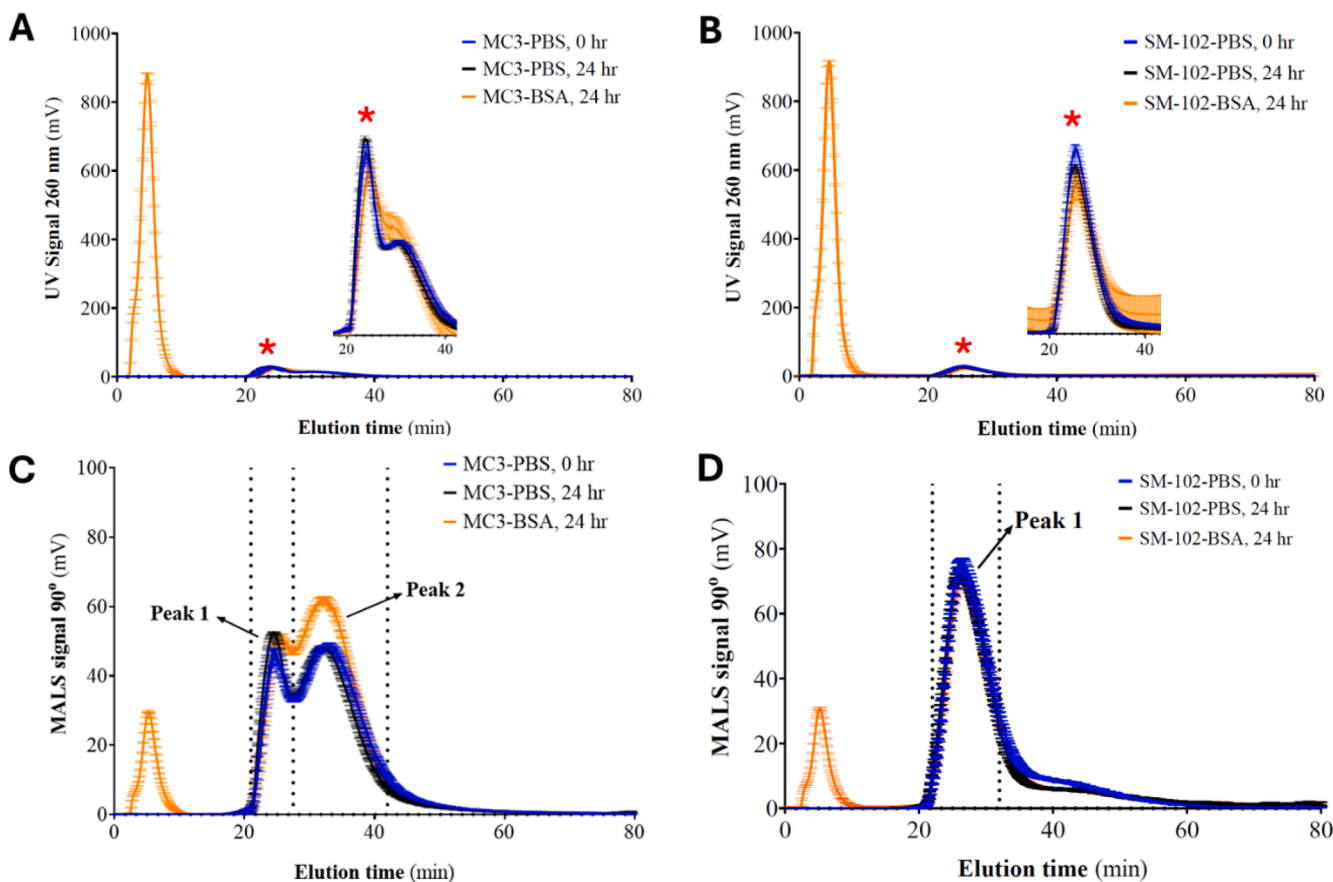

Fig. 2. FI-AF4-UV-MALS fractograms for (A) MC3-LNPs (control) and MC3-LNPs incubated in 35 mg/mL Bovine Serum Albumin (BSA), (B) SM-102 LNPs, (C) MALS fractograms (90°) plotted for peak 1 and peak 2 for MC3-LNPs incubated in 35 mg/mL BSA, (D) SM-102 LNPs. Time-points indicate 0 hour (control) and 24 h incubation at 37 °C. Error bars represent ± *S*.D mean of triplicate injections. The peaks marked with a red asterisk (*) show enlarged peaks. Vertical dashed lines indicate peak region of interest.
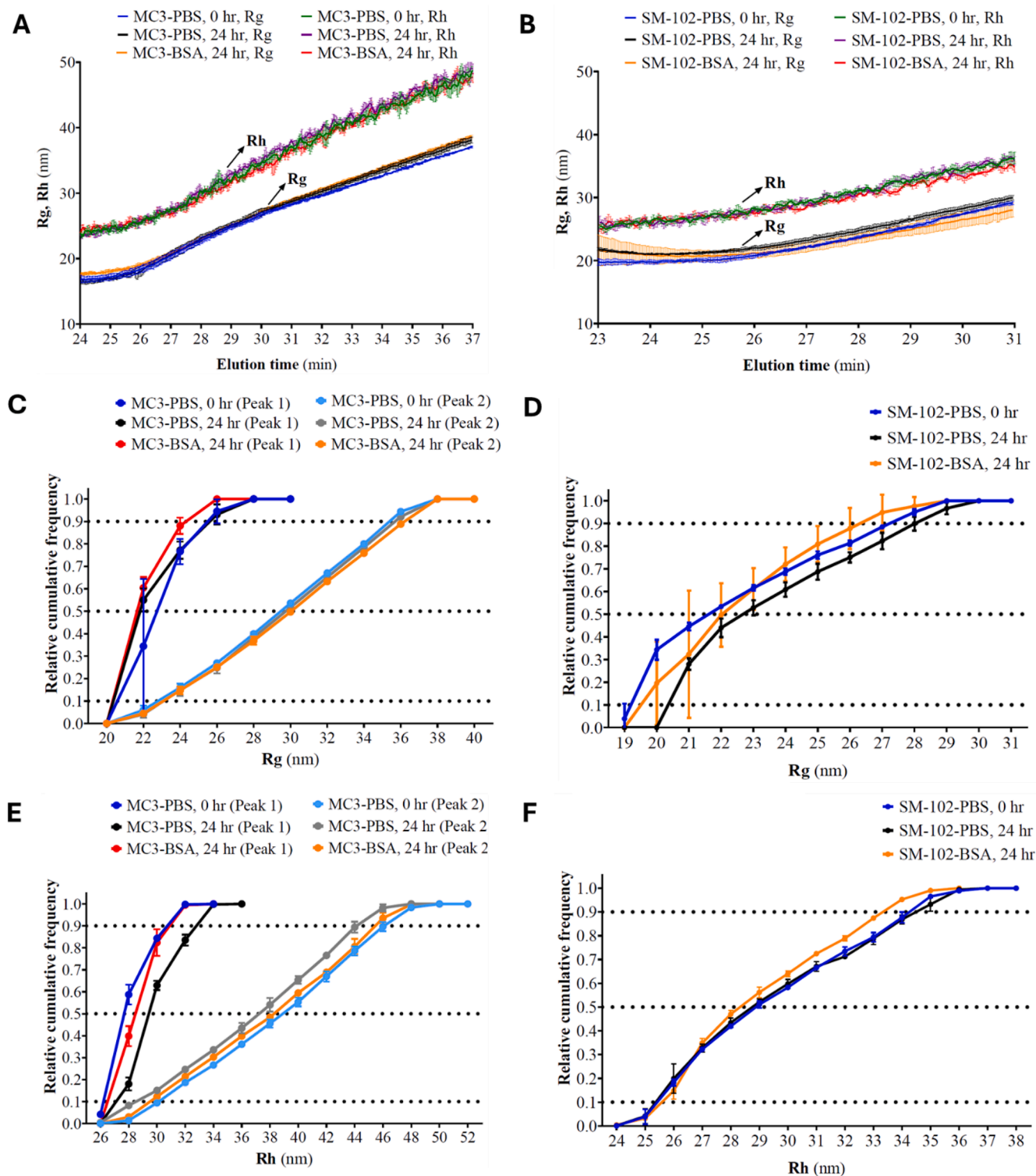
Fig. 3. Radius of gyration (R_g) and hydrodynamic radius (R_h)obtained by obtained by FI-AF-MALS-DLS for (A) MC3-LNPs incubated in 35 mg/mL BSA, (B) SM-102 LNPs (C) R_g distribution RG10, RG50, RG90 corresponding to the percentages 10 %, 50 % and 90 % respectively of LNPs under the reported R_g value for MC3 LNPs, (D) SM-102 LNPs (E) R_h distribution RH10, RH50, RH90 corresponding to the percentages 10 %, 50 % and 90 % respectively of LNPs under the reported R_h value for MC3 LNPs, (F) SM-102 LNPs. Time-points indicate 0 hour (control) and 24 h incubation at 37 °C. Error bars represent $\pm$ S.D mean of triplicate injections.

distribution of mass towards the surface of the particle. Upon interaction with BSA, the shape factor of SM-102 LNPs decreased at 24 h, remaining constant across the peak at 0.806 $\pm$ 0.012 for SM-102 LNPs, and 0.783 $\pm$ 0.034 for SM-102-BSA at 24 h with no significant difference between the shape factors (Fig. 4B and **Table S4**). In contrast, the shape factor increased for MC3-LNPs, with a higher value for sub-peak 2 (0.769 $\pm$

0.011 for MC3-LNPs, and 0.795 $\pm$ 0.004 for MC3-BSA for 24 h) compared to sub-peak 1 (0.713 $\pm$ 0.018 for MC3-LNPs and 0.741 $\pm$ 0.006 for MC3-BSA) (Fig. 4A and **Table S4**). The cumulative shape factor distribution (SF) for both LNP prototypes was evaluated for their 10, 50 and 90th percentile (Fig. 5). Fig. 5E-F show no significant differences in SF10, SF50 and SF90 between different incubations, however
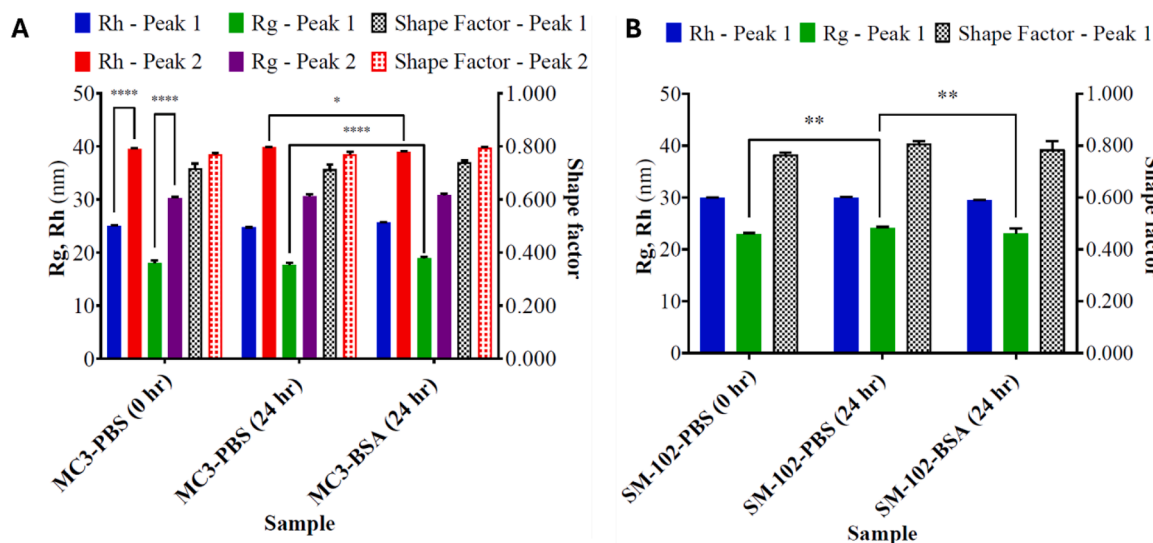
Fig. 4. Average radius of gyration (R_g), hydrodynamic radius (R_h) and shape factor (R_g/R_h) calculated from peaks integrated in Fig. 3. Plots represent (A) MC3 LNPs incubated in PBS (control) and in 35 mg/mL BSA (B)SM-102 LNPs. Time-points indicate 0 hour (control) and 24 h incubation at 37 °C. Statistical analysis was performed using one-way ANOVA followed by post-hoc Tukey's test. Error bars represent $\pm$ *S*.D mean of triplicate injections, *$p < 0.05$, **$p < 0.01$, ****$p < 0.0001$. Refer to Table S4 for R_g, R_h and shape factor values and Figure S5 for Tukey's test sample comparisons.

the differences are still meaningful. MC3-BSA showed a higher 90th percentile shape factor for both peak 1 (0.762 ± 0.007) and peak 2 (0.804 ± 0.004) compared to MC3-PBS incubation at 24 h for peak 1 (0.753 ± 0.006) and peak 2 (0.780 ± 0.009). In contrast, SM-102-BSA at 24 h exhibited a lower SF90 (0.804 ± 0.045) compared to SM-102 LNPs at 24 h (0.823 ± 0.012).

4. Discussion

LNP characterisation with AF4 has been explored in previous studies [18,20,33], but this study is the first to direct the significance of different lipid choices and their differential impact on LNP protein corona formation for SM-102 and MC3 LNPs. AF4 offers high resolution separation and inline analysis of particles, which is crucial for characterizing the protein corona with minimal perturbation of the LNP-protein complex. The low-shear separation allows for gentle handling of the LNP-protein interactions, preserving their morphology.

In this study, we used parameters such as the R_h, R_g and shape factor to evaluate these interactions. The AF4 separation at low PDI ($\sim$0.1) and specific peak selection make the hydrodynamic size measured by AF4 more reliable for studying the protein corona. The shape factor, which indicates deviation from spherical conformation, was useful for assessing BSA binding [21,34] as it indicates a deviation from the spherical conformation of the LNP or confirms retention of the spherical conformation with higher mass distributed towards the edge of the nanoparticle. Assuming protein adsorption occurs at the periphery will result in a larger increase in R_g relative to R_h, resulting in an increase in shape factor. This is based on the assumption that the density of BSA is higher than the average density of the LNP. In the case of MC3, the increase in shape factor with both sub-peaks 1 and 2 indicates BSA binding on the surface resulting in shifts to a spherical conformation. Conversely, with SM-102 LNPs, the decreased shape factor following BSA incubation, indicates a restructuring of the internal architecture of LNPs resulting in a denser core. This LNP restructuring may also be evident from significant differences in measured mean radii and the differences in the 90 % variant for both R_g and R_h following BSA adsorption. This restructuring is emphasised from the cumulative distribution plots for R_g comparing MC3 and SM-102 prototypes. Although, the same protein has been used for studying protein corona formation, significant differences between LNP control and the protein corona were only evident in the case of MC3

LNPs. The differences in shape factor values can be attributed to differences in ionisable lipid composition; SM-102 lipid contains a branched tail and extended aliphatic branches similar to multi-tail structures, whilst MC3 contains unsaturated linear chains. This renders different packing geometries, with a cylindrical geometry in the case of MC3 and cone-shape geometry for SM-102. [20] The lipid packing results in different surface chemistries leading to different interactions with BSA.

Both MC3 and SM-102 LNPs manufactured in this study contain polyethylene glycol (PEG)ylated lipid, which is widely used as an anti-opsonization strategy. PEG increases surface hydrophilicity and forms protrusions on the nanoparticle surface, which plays a critical role in hindering interactions between nanoparticles and opsonins. [35] This explains why the size and conformational properties of LNPs were not significantly altered following LNP incubation with BSA. The MC3 LNP prototype fractograms show two peaks, which are not fully resolved. Although peak 2 can be treated as a sub-population of larger LNP size, high-resolution AF4 characterisation indicated the presence of other lipid-based nanoparticles contributing to the second sub-peak, giving rise to different size (R_g, R_h), morphology (shape factor) and light scattering properties. Previous findings have shown that PEG-shedding following intravenous (i.v.) administration enables LNPs to fuse with endosomal membranes and release their cargo. [35] PEG-shedding has also been demonstrated following the induction of anti-PEG IgM as a useful means of controlling LNP interactions with cellular components. [36]

Proteins can undergo conformational changes upon interaction with nanoparticles [37]. Protein secondary structures include alpha-helices and beta-sheets stabilised by various non-covalent interactions, tmay unfold and expose different regions upon surface adsorption onto LNPs. [38] This unfolding can be influenced by the surface properties of the LNPs, including their hydrophilicity and charge. For example, BSA may unfold and expose its hydrophobic and opposite charges when interacting with LNPs. [39] It cannot be assumed that upon BSA adsorption on the LNP surface, that BSA remains folded resulting in an increase in R_g and R_h of the protein corona. The complexity in protein unfolding renders determination of the formation of the protein corona challenging. These results demonstrate the power of AF4 as a technique for probing the interactions between LNP prototypes with binary protein systems, providing detailed information on physicochemical attribute
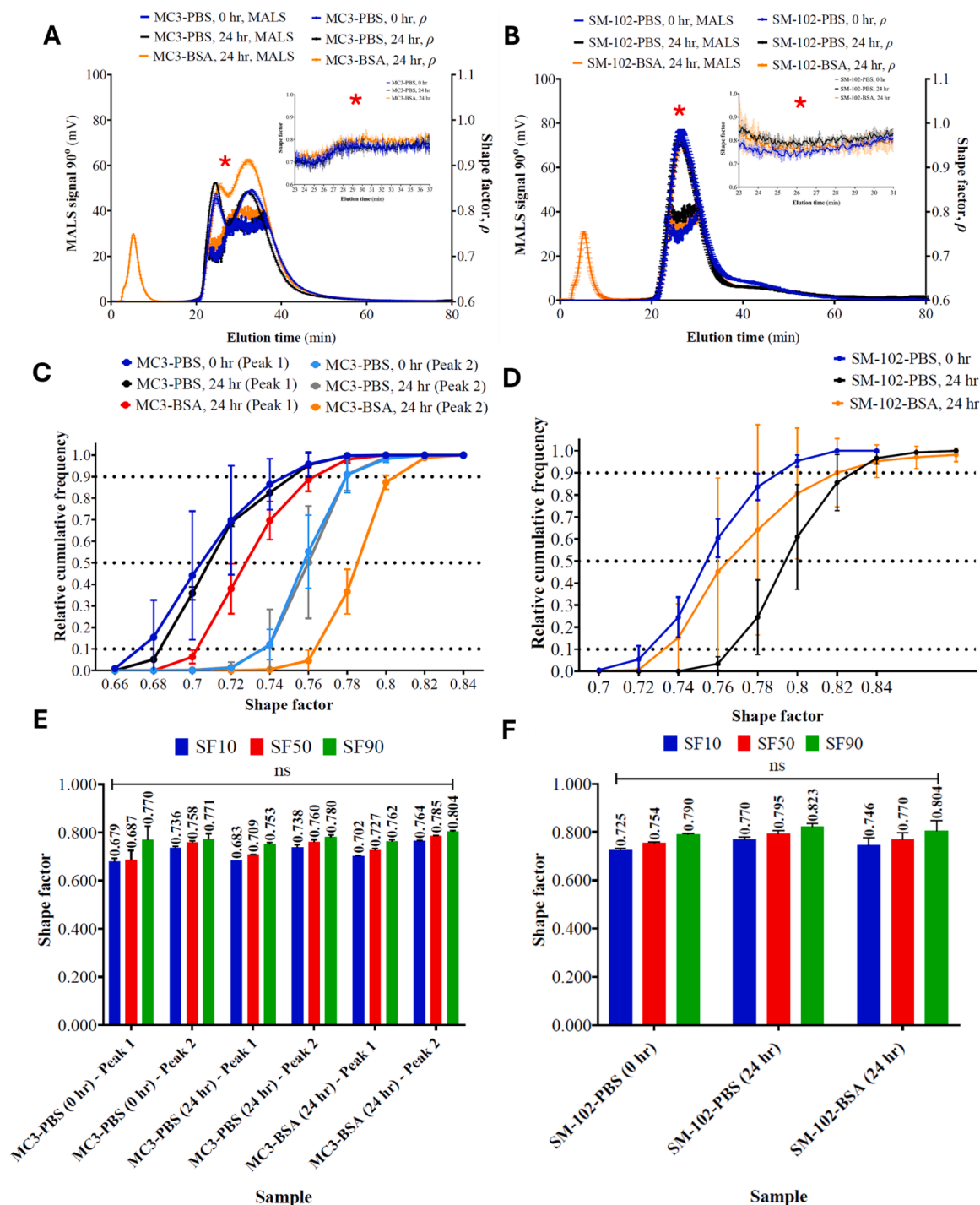
Fig. 5. Shape factor obtained by FI-AF-MALS-DLS. Plots represent (A) simultaneous MALS (90°) signal and shape factor for MC3-LNPs incubated in PBS (control) and 35 mg/mL BSA, (B) SM-102 LNPs, (C) shape factor distribution for shape factor (SF) SF10, SF50, SF90 corresponding to the percentages 10 %, 50 % and 90 % of LNPs under the reported shape factor value for MC3 LNPs, (D) SM-102 LNPs, (E) statistical analysis using one-way ANOVA followed by post-hoc Tukey's test comparing the 10, 50, and 90th percentile (SF10, SF50 and SF90) between incubation, (F) SM-102 LNPs. Time-points indicate 0 hour (control) and 24 h incubation at 37 °C. Error bars which represent $\pm$ S.D mean of triplicate injections. ns; not significant. Refer to Figure S6 for Tukey's test sample comparisons. The peaks marked with a red asterisk (*) show enlarged shape factor trace. Abbreviations: ns: not significant, SF: shape factor.

changes upon exposure to protein-containing media. Further, complementary orthogonal techniques can be used for the *in situ* analysis of corona complexes, followed by downstream analysis using a variety of techniques such as liquid chromatography-tandem mass spectrometry (LC-MS/MS), [40] fluorescence-based techniques, [41–43] isothermal titration calorimetry (ITC), [44] and circular dichroism (CD) spectroscopy. [45,46]

5. Conclusions

In this work, AF4 characterisation of SM-102 and MC3 LNPs in the presence of BSA was performed as an approach to recover LNPs from bulk biological media. This study presents an opportunity to advance research on LNP interactions with biological matrices, paving the way for new developments in RNA-based drug delivery systems. Although

BSA has been used as the model biomolecules and two LNP prototypes, the versatility of AF4 makes it suitable for handling different LNP prototypes and biomolecules ensuring sample integrity. The integration of high-resolution, robust analytical techniques in the characterization of nanomedicine paves the way for future evaluation of novel lipids and LNP manufacturing technologies.

Data availability

DOI for dataset to be provided at the end of the manuscript. All manuscript data are available to download from https://doi.org/10.15129/02457dcc-f32b-4528-900b-14dacd9c4e69

CRediT authorship contribution statement

Rand Abdulrahman: Writing – review & editing, Writing – original draft, Methodology, Investigation, Formal analysis, Data curation, Conceptualization. **Panida Punnabhum:** Writing – original draft, Formal analysis, Data curation, Conceptualization. **Robin Capomaccio:** Writing – review & editing, Supervision, Funding acquisition, Formal analysis, Conceptualization. **Kevin Treacher:** Writing – review & editing, Supervision, Funding acquisition. **Yvonne Perrie:** Writing – review & editing, Supervision, Conceptualization. **Zahra Rattray:** Writing – review & editing, Writing – original draft, Supervision, Project administration, Investigation, Funding acquisition, Formal analysis, Conceptualization.

Declaration of competing interest

The authors declare the following financial interests/personal relationships which may be considered as potential competing interests:

Zahra Rattray reports financial support was provided by AstraZeneca UK Limited. Zahra Rattray reports financial support was provided by Engineering and Physical Sciences Research Council. Robin Capomaccio, Kevin Treacher reports a relationship with AstraZeneca UK Limited that includes: employment and stock ownership. If there are other authors, they declare that they have no known competing financial interests or personal relationships that could have appeared to influence the work reported in this paper.

Acknowledgements

Supplementary materials

Supplementary material associated with this article can be found, in the online version, at doi:10.1016/j.chroma.2025.465663.

References

[1] H.H. Ly, S. Daniel, S.K.V. Soriano, Z. Kis, A.K. Blakney, Optimization of lipid nanoparticles for saRNA expression and cellular activation using a design-of-experiment approach, Mol. Pharm 19 (6) (2022) 1892–1905.

[2] K. Paunovska, C.D. Sago, C.M. Monaco, W.H. Hudson, M.G. Castro, T.G. Rudoltz, S. Kalathoor, D.A. Vanover, P.J. Santangelo, R. Ahmed, A.V. Bryksin, J.E. Dahlman, A direct comparison of in vitro and in vivo nucleic acid delivery mediated by hundreds of nanoparticles reveals a weak correlation, Nano. Lett 18 (3) (2018) 2148–2157.

[3] D.N. Trinh, M. Radlinskaite, J. Cheeseman, G. Kuhnle, H.M.I. Osborn, P. Meleady, D.I.R. Spencer, M.P. Monopoli, Biomolecular corona stability in association with plasma cholesterol level, Nanomaterials. (Basel) (15) (2022) 12.

[4] D. Pozzi, G. Caracciolo, L. Digiacomo, V. Colapicchioni, S. Palchetti, A.L. Capriotti, C. Cavaliere, R. Zenezini Chiozzi, A. Puglisi, A. Lagana, The biomolecular corona of nanoparticles in circulating biological media, Nanoscale 7 (33) (2015) 13958–13966.

[5] P. Aggarwal, J.B. Hall, C.B. McLeland, M.A. Dobrovolskaia, S.E. McNeil, Nanoparticle interaction with plasma proteins as it relates to particle biodistribution, biocompatibility and therapeutic efficacy, Adv. Drug. Deliver. Rev 61 (6) (2009) 428–437.

[6] D. Walczyk, F.B. Bombelli, M.P. Monopoli, I. Lynch, K.A. Dawson, What the cell "sees" in bionanoscience, J. Am. Chem. Soc. 132 (16) (2010) 5761–5768.

[7] Z.J. Deng, M. Liang, M. Monteiro, I. Toth, R.F. Minchin, Nanoparticle-induced unfolding of fibrinogen promotes Mac-1 receptor activation and inflammation, Nat. Nanotechnol 6 (1) (2011) 39–44.

[8] C.D. Walkey, W.C. Chan, Understanding and controlling the interaction of nanomaterials with proteins in a physiological environment, Chem. Soc. Rev 41 (7) (2012) 2780–2799.

[9] M. Debnath, J. Forster 3rd, A. Ramesh, A. Kulkarni, Protein corona formation on lipid nanoparticles negatively affects the NLRP3 inflammasome activation, Bioconjug. Chem 34 (10) (2023) 1766–1779.

[10] S.C. Semple, A. Akinc, J. Chen, A.P. Sandhu, B.L. Mui, C.K. Cho, D.W. Sah, D. Stebbing, E.J. Crosley, E. Yaworski, I.M. Hafez, J.R. Dorkin, J. Qin, K. Lam, K. G. Rajeev, K.F. Wong, L.B. Jeffs, L. Nechev, M.L. Eisenhardt, M. Jayaraman, M. Kazem, M.A. Maier, M. Srinivasulu, M.J. Weinstein, Q. Chen, R. Alvarez, S. A. Barros, S. De, S.K. Klimuk, T. Borland, V. Kosovrasti, W.L. Cantley, Y.K. Tam, M. Manoharan, M.A. Ciufolini, M.A. Tracy, A. de Fougerolles, I. MacLachlan, P. R. Cullis, T.D. Madden, M.J. Hope, Rational design of cationic lipids for siRNA delivery, Nat. Biotechnol 28 (2) (2010) 172–176.

[11] A. Akinc, W. Querbes, S. De, J. Qin, M. Frank-Kamenetsky, K.N. Jayaprakash, M. Jayaraman, K.G. Rajeev, W.L. Cantley, J.R. Dorkin, J.S. Butler, L. Qin, T. Racie, A. Sprague, E. Fava, A. Zeigerer, M.J. Hope, M. Zerial, D.W. Sah, K. Fitzgerald, M. A. Tracy, M. Manoharan, V. Koteliansky, A. Fougerolles, M.A. Maier, Targeted delivery of RNAi therapeutics with endogenous and exogenous ligand-based mechanisms, Mol. Ther 18 (7) (2010) 1357–1364.

[12] Agency, E.M. *Spikevax - summary of product characteristics*; 2021.

[13] Agency., E.M., Onpattro - summary of product characteristics. 2018.

[14] Standardization, E.C.F., Nanotechnologies — analysis of nano-objects using asymmetrical-flow and centrifugal field-flow fractionation. 1 ed.; 2021.

[15] M. Klein, M. Menta, T.G. Dacoba, J. Crecente-Campo, M.J. Alonso, D. Dupin, I. Loinaz, B. Grassl, F. Seby, Advanced nanomedicine characterization by DLS and AF4-UV-MALS: application to a HIV nanovaccine, J. Pharm. Biomed. Anal 179 (2020) 113017.

[16] M. McEvoy, V. Razinkov, Z. Wei, J.R. Casas-Finet, G.I. Tous, M.A. Schenerman, Improved particle counting and size distribution determination of aggregated virus populations by asymmetric flow field-flow fractionation and multiangle light scattering techniques, Biotechnol. Prog 27 (2) (2011) 547–554.

[17] T.J. Evjen, S. Hupfeld, S. Barnert, S. Fossheim, R. Schubert, M. Brandl, Physicochemical characterization of liposomes after ultrasound exposure - mechanisms of drug release, J. Pharm. Biomed. Anal 78-79 (2013) 118–122.

[18] J. Parot, D. Mehn, H. Jankevics, N. Markova, M. Carboni, C. Olaisen, A.D. Hoel, M. S. Sigfusdottir, F. Meier, R. Drexel, G. Vella, B. McDonagh, T. Hansen, H. Bui, G. Klinkenberg, T. Visnes, S. Gioria, P. Urban-Lopez, A. Prina-Mello, S.E. Borgos, F. Caputo, L. Calzolai, Quality assessment of LNP-RNA therapeutics with orthogonal analytical techniques, J. Control Release 367 (2024) 385–401.

[19] F. Caputo, A. Arnould, M. Bacia, W.L. Ling, E. Rustique, I. Texier, A.P. Mello, A. C. Couffin, Measuring particle size distribution by asymmetric flow field flow fractionation: a powerful method for the preclinical characterization of lipid-based nanoparticles, Mol. Pharm 16 (2) (2019) 756–767.

[20] R. Mildner, S. Hak, J. Parot, A. Hyldbakk, S.E. Borgos, D. Some, C. Johann, F. Caputo, Improved multidetector asymmetrical-flow field-flow fractionation method for particle sizing and concentration measurements of lipid-based nanocarriers for RNA delivery, Eur. J. Pharm. Biopharm 163 (2021) 252–265.

[21] Y. Hu, R.M. Crist, J.D. Clogston, The utility of asymmetric flow field-flow fractionation for preclinical characterization of nanomedicines, Anal. Bioanal. Chem 412 (2) (2020) 425–438.

[22] K. Daramy, P. Punnabhum, M. Hussain, C. Minelli, Y. Pei, N.J.W. Rattray, Y. Perrie, Z. Rattray, Nanoparticle isolation from biological media for protein corona analysis: the impact of incubation and recovery protocols on nanoparticle properties, J. Pharm. Sci (2023).

[23] L. Bohmert, L. Voss, V. Stock, A. Braeuning, A. Lampen, H. Sieg, Isolation methods for particle protein corona complexes from protein-rich matrices, Nanoscale. Adv 2 (2) (2020) 563–582.

[24] S. Kim, J.H. Kim, S. Kim, J.S. Park, B.S. Cha, E.S. Lee, J. Han, J. Shin, Y. Jang, K. S. Park, Loop-mediated isothermal amplification-based nucleic acid lateral flow assay for the specific and multiplex detection of genetic markers, Anal. Chim. Acta 1205 (2022) 339781.

[25] W.S. Jang, J.M. Lee, E. Lee, S. Park, C.S. Lim, Loop-mediated isothermal amplification and lateral flow immunochromatography technology for rapid diagnosis of influenza A/B, Diagnostics. (Basel) (9) (2024) 14.

[26] S. Agarwal, C. Warmt, J. Henkel, L. Schrick, A. Nitsche, F.F. Bier, Lateral flow-based nucleic acid detection of SARS-CoV-2 using enzymatic incorporation of biotin-labeled dUTP for POCT use, Anal. Bioanal. Chem 414 (10) (2022) 3177–3186.

[27] I.V. Safenkova, M.V. Kamionskaya, A.V. Zherdev, B.B. Dzantiev, Evaluation of amplicons by AF4 as assistant for deep comprehension of loop-mediated isothermal amplification combined with lateral flow assay, J. Chromatogr. A 1739 (2025) 465528.

[28] Y. Suzuki, H. Ishihara, Difference in the lipid nanoparticle technology employed in three approved siRNA (Patisiran) and mRNA (COVID-19 vaccine) drugs, Drug. Metab. Pharmacokinet 41 (2021) 100424.

[29] B. Binici, Z. Rattray, A. Schroeder, Y. Perrie, The role of biological sex in pre-clinical (Mouse) mRNA vaccine studies, Vaccines. (Basel) 12 (3) (2024).

[30] A.K. Leung, Y.Y. Tam, S. Chen, I.M. Hafez, P.R. Cullis, Microfluidic mixing: a general method for encapsulating macromolecules in lipid nanoparticle systems, J. Phys. Chem. B 119 (28) (2015) 8698–8706.

[31] J.A. Kulkarni, M.M. Darjuan, J.E. Mercer, S. Chen, R. van der Meel, J.L. Thewalt, Y. Y.C. Tam, P.R. Cullis, On the formation and morphology of lipid nanoparticles containing ionizable cationic lipids and siRNA, ACS Nano 12 (5) (2018) 4787–4795.

[32] S. Patel, R.C. Ryals, K.K. Weller, M.E. Pennesi, G. Sahay, Lipid nanoparticles for delivery of messenger RNA to the back of the eye, J. Control Release 303 (2019) 91–100.

[33] M.A. Graewert, C. Wilhelmy, T. Bacic, J. Schumacher, C. Blanchet, F. Meier, R. Drexel, R. Welz, B. Kolb, K. Bartels, T. Nawroth, T. Klein, D. Svergun, P. Langguth, H. Haas, Quantitative size-resolved characterization of mRNA nanoparticles by in-line coupling of asymmetrical-flow field-flow fractionation with small angle X-ray scattering, Sci. Rep 13 (1) (2023) 15764.

[34] F. Caputo, D. Mehn, J.D. Clogston, M. Rosslein, A. Prina-Mello, S.E. Borgos, S. Gioria, L. Calzolai, Asymmetric-flow field-flow fractionation for measuring particle size, drug loading and (in)stability of nanopharmaceuticals. The joint view of European Union Nanomedicine Characterization Laboratory and National Cancer Institute - Nanotechnology Characterization Laboratory, J. Chromatogr. A 1635 (2021) 461767.

[35] K. Partikel, R. Korte, N.C. Stein, D. Mulac, F.C. Herrmann, H.U. Humpf, K. Langer, Effect of nanoparticle size and PEGylation on the protein corona of PLGA nanoparticles, Eur. J. Pharm. Biopharm 141 (2019) 70–80.

[36] T. Suzuki, Y. Suzuki, T. Hihara, K. Kubara, K. Kondo, K. Hyodo, K. Yamazaki, T. Ishida, H. Ishihara, PEG shedding-rate-dependent blood clearance of PEGylated lipid nanoparticles in mice: faster PEG shedding attenuates anti-PEG IgM production, Int. J. Pharm 588 (2020) 119792.

[37] M. Rabe, D. Verdes, S. Seeger, Understanding protein adsorption phenomena at solid surfaces, Adv. Colloid Interface. Sci 162 (1) (2011) 87–106.

[38] D. Leckband, J. Israelachvili, Intermolecular forces in biology, Q. Rev. Biophys 34 (2) (2001) 105–267.

[39] X. Wang, R. Lei, L. Li, X. Fei, R. Ju, X. Sun, H. Cao, Q. Zhang, C. Chen, X. Wang, Rearrangement of protein structures on a gold nanoparticle surface is regulated by ligand adsorption modes, Nanoscale 13 (48) (2021) 20425–20436.

[40] C.C. Fleischer, C.K. Payne, Secondary structure of corona proteins determines the cell surface receptors used by nanoparticles, J. Phys. Chem. B 118 (49) (2014) 14017–14026.

[41] M. Martinez-Moro, D. Di Silvio, S.E. Moya, Fluorescence correlation spectroscopy as a tool for the study of the intracellular dynamics and biological fate of protein corona, Biophys. Chem. 253 (2019) 106218.

[42] L.X. Gao, H. Hao, Y.Q. Yu, J.L. Chen, W.Q. Chen, Z.D. Gong, Y. Liu, F.L. Jiang, Protein labeling facilitates the understanding of protein corona formation via fluorescence resonance energy transfer and fluorescence correlation spectroscopy, Langmuir 39 (43) (2023) 15275–15284.

[43] C. Rocker, M. Potzl, F. Zhang, W.J. Parak, G.U. Nienhaus, A quantitative fluorescence study of protein monolayer formation on colloidal nanoparticles, Nat. Nanotechnol 4 (9) (2009) 577–580.

[44] J. Muller, D. Prozeller, A. Ghazaryan, M. Kokkinopoulou, V. Mailander, S. Morsbach, K. Landfester, Beyond the protein corona - lipids matter for biological response of nanocarriers, Acta. Biomater 71 (2018) 420–431.

[45] J.S. Yoneda, M.B. Cardoso, Nanoparticle-induced conformational changes in protein corona revealed by circular dichroism spectroscopy, Nanomedicine. (Lond) 18 (9) (2023) 709–711.

[46] S. Li, Z. Peng, R.M. Leblanc, Method to determine protein concentration in the protein-nanoparticle conjugates aqueous solution using circular dichroism spectroscopy, Anal. Chem 87 (13) (2015) 6455–6459.